

Clocking the Onset of Bilayer Coherence in a High- T_C Cuprate Supplemental Material

Edoardo Baldini,^{1,2} Andreas Mann,¹ Benjamin P. P. Mallett,³ Christopher Arrell,² Frank van Mourik,² Thomas Wolf,⁴ Dragan Mihailovic,⁵ Jeffrey L. Tallon,⁶ Christian Bernhard,³ José Lorenzana,⁷ and Fabrizio Carbone¹

¹Laboratory for Ultrafast Microscopy and Electron Scattering, IPHYS, EPFL, CH-1015 Lausanne, Switzerland

²Laboratory of Ultrafast Spectroscopy, ISIC, EPFL, CH-1015 Lausanne, Switzerland

³Department of Physics, University of Fribourg, Chemin du Musée 3, CH-1700 Fribourg, Switzerland

⁴Institute of Solid State Physics, Karlsruhe Institute of Technology, Postfach 3640, Karlsruhe 76021, Germany

⁵Jozef Stefan Institute and International Postgraduate School, Jamova 39, SI-1000 Ljubljana, Slovenia

⁶Robinson Research Institute, Victoria University of Wellington, P.O. Box 33436 Lower Hutt, New Zealand

⁷Institute for Complex Systems - CNR, and Physics Department,
University of Rome "La Sapienza", I-00185 Rome, Italy

(Dated: December 11, 2016)

S1. METHODS

A. Sample growth and preparation.

A high quality $\text{NdBa}_2\text{Cu}_3\text{O}_{6+x}$ (NBCO) single-crystal was flux-grown in an Y-stabilized zirconia crucible and under low oxygen partial pressure to avoid spurious substitution of the Nd ion onto the Ba site¹. The resulting crystal is a parallelepiped with dimensions $5.5 \text{ mm} \times 4 \text{ mm} \times 1 \text{ mm}$ along the a , b and c axes respectively. The sample was annealed in oxygen for ten days at 370°C resulting in a superconducting transition temperature of $T_C = 93.5 \text{ K}$, as measured by dc magnetisation, and a sharp transition width of 1.5 K . The crystal surfaces were mechanically polished to optical grade using diamond powder paste.

B. Broadband spectroscopic ellipsometry.

Using broadband ellipsometry, we measured the c -axis and in-plane complex optical conductivity of the sample, covering the spectral range from 12.5 meV to 6.0 eV . Anisotropy corrections were performed using standard numerical procedures^{2,3} and diffraction effects at low frequency were accounted for using the procedure developed by Humlíček *et al.*⁴. We used a home-built ellipsometer attached to a Bruker fast-Fourier spectrometer at the infrared beam line of the ANKA synchrotron at the Karlsruhe Institute for Technology to measure from 12.5 meV to 85.0 meV ² and a Woollam VASE ellipsometer at the University of Fribourg for 0.5 eV to 6.0 eV . When at cryogenic temperatures, the latter measurements were performed in a vacuum better than 10^{-8} mbar to prevent measurable ice-condensation onto the sample.

C. Ultrafast broadband optical spectroscopy.

Femtosecond broadband transient reflectivity experiments have been performed using a set-up described in detail in Ref.⁵. A cryogenically-cooled amplified laser

system provided sub-50 fs pulses centred around 1.55 eV at a repetition rate of 6 kHz . One third of the output, representing the probe beam, was focused on a CaF_2 cell to generate broadband visible pulses with a bandwidth covering the spectral range between 1.70 eV and 2.80 eV . The probe beam was then collimated and focused onto the sample through a pair of parabolic mirrors. The remaining two thirds of the output of the amplifier, representing the pump beam, were directed towards the sample under normal incidence. Along the pump path a chopper with a 60 slot plate was inserted, operating at 1.5 kHz and phase-locked to the laser-system. The polarizations for both the pump and the probe beam were set along the $[110]$ crystallographic direction, giving access to the in-plane optical response of the sample and selecting the $A_{1g} + B_{2g}$ Raman symmetry configuration. Pump and probe were focused onto the sample with spatial dimensions of $120 \mu\text{m} \times 87 \mu\text{m}$ and $23 \mu\text{m} \times 23 \mu\text{m}$, respectively. The sample was mounted inside the chamber of a closed cycle cryostat, which provides a temperature-controlled environment in the range $10 - 340 \text{ K}$. The measurements were performed in a vacuum better than 10^{-7} mbar and several temperature cycles have been applied to prevent measurable ice-condensation onto the sample. The reflected probe beam was dispersed by a fiber-coupled 0.3 m spectrograph and detected on a shot-to-shot basis with a CMOS linear array.

S2. FAR-INFRARED ELLIPSOMETRY

We estimate the T_C and T^* temperature scales from the analysis of the real (σ_1) part of the c -axis conductivity, as measured by steady-state ellipsometry in the far-infrared spectral region. The data are reported in Fig. 2(a) of the main text. For our purposes, in the present analysis, we only focus on the evaluation of the spectral weight (SW) in the $12.5 - 85.0 \text{ meV}$ spectral region as a function of temperature. We calculate the SW as:

$$SW = \int_{12.5\text{meV}}^{85\text{meV}} \sigma_{1,c}(\omega) d\omega \quad (1)$$

In Fig. S1 the temperature dependence of the SW is shown. As expected, we observe that the SW decreases well above T_C . This ‘missing’ SW is a characteristic feature of the pseudogap⁶ and provides an estimate of T^* . According to our data, we can determine $T_C \sim 94$ K and $T^* \sim 170$ K, as indicated in Fig. S1.

S3. VISIBLE ELLIPSOMETRY

The in-plane optical conductivity of the sample was also measured by means of broadband spectroscopic ellipsometry from the near-infrared to the ultraviolet. In Fig. S2(a), the spectrum of the real part of the optical conductivity $\sigma_{1,ab}(\omega)$ is reported as a function of temperature. The energy of the monochromatic pump (red arrow) and of the broadband probe (grey shaded area), used in the nonequilibrium experiment, are highlighted. The measured response agrees well with previously reported data for the 123 family of cuprates^{7,8}.

The spectral range below 1 eV has been modeled in the past including a Drude-like contribution and a mid-infrared component⁷. The feature at 1.40 eV sharpens when temperature decreases and is closely followed by a weaker satellite at 1.77 eV; it has been ascribed to a charge-transfer excitation in the CuO_2 planes and represents a reminiscence of the fundamental absorption gap visible in the same region of the conductivity in the undoped parent compound. Similar features appear in $\text{La}_{2-x}\text{Sr}_x\text{CuO}_4$ and have been assigned to stripe related bands⁹. A second prominent peak can be observed around 2.60 eV, which progressively loses weight with decreasing temperature. Linear Muffin-Tin Orbital calcu-

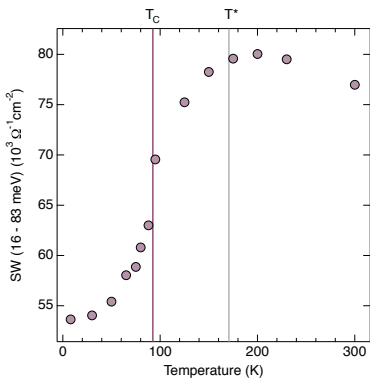


FIG. S1. Temperature dependence of the c-axis spectral weight, calculated over the far-infrared spectral range covered by spectroscopic ellipsometry (12.5 - 85.0 meV). The violet and grey vertical lines mark the estimated T_C and T^* respectively.

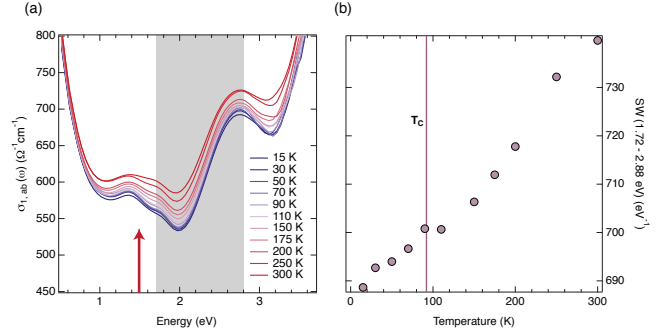


FIG. S2. (a) Real part of the in-plane optical conductivity at selected temperatures. The red arrow indicates the photon energy of the pump pulse used in the nonequilibrium experiment, while the grey shaded area refers to the spectral range monitored by the broadband probe pulse. (b) Temperature evolution of the spectral weight calculated over the region highlighted by the grey shaded area (1.72 - 2.88 eV). T_C is indicated on the figure as a violet vertical line.

lations assigned this peak to an interband transition into the antibonding $\text{Cu}(2)\text{-O}(2)\text{-O}(3)$ band, with the initial state being found in a manifold of strongly dispersive bands¹⁰. This interpretation has been recently refined by Dynamical Mean Field Theory calculations, which described it as a charge excitation from the Lower Hubbard Band (LHB) to E_F in OP YBCO¹¹. Figure S2(b) shows the partial SW integrated over the region covered by the grey shaded area (1.72 - 2.88 eV) as a function of temperature. We observe that the partial SW drops with decreasing temperature and reveals a kink around T_C . No features are instead seen between T_C and T^* . The observation of peculiar effects at T_C taking place in the equilibrium optical spectra at high-energies has been provided by several studies in the past^{8,12-14} and interpreted as a fingerprint of Mottness^{15,16}.

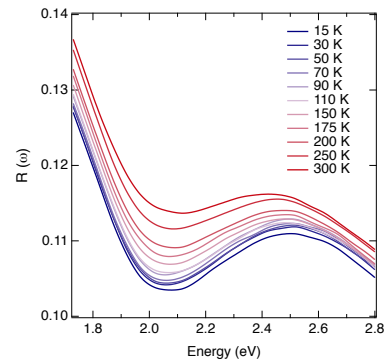


FIG. S3. Temperature dependence of the in-plane reflectance, $R(\omega)$, as calculated from the spectroscopic ellipsometry data. The displayed spectral range is limited to the one of the pump-probe experiment.

Finally, we comment on the equilibrium reflectance $R(\omega)$, that can be calculated from our spectroscopic ellipsometry data. Figure S3 displays the steady-state reflectance as a function of temperature, limited in the spectral range that is probed by our nonequilibrium experiment (1.73 - 2.80 eV). We observe that, for increasing temperature, $R(\omega)$ increases its value in the whole spectral range. This confirms that the negative ultrafast response measured by the pump-probe experiment has a nonthermal origin.

S4. BROADBAND TRANSIENT REFLECTIVITY

A. Fluence dependence

Before performing a detailed temperature dependence, a compromise between the data acquisition rate and the intensity of the laser pump pulse has to be found. Indeed, high signal-to-noise ratio at all temperatures is desirable, but the pump intensity should be maintained below the threshold for the complete vaporization of the condensate below T_C . To this end, we perform a fluence dependence of the in-plane $\Delta R/R$ for establishing the suitable fluence to be used in the temperature dependence. We first check the linearity of the response by positioning the delay stage on the maximum of the $\Delta R/R$ signal at specific probe photon energies and varying the incident fluence on the sample. We identify the absorbed fluence of 0.35 mJ/cm^2 as the highest one at which the response maintains linearity in the SC state. Based on the above arguments, we choose an absorbed fluence of 0.3 mJ/cm^2 to perform the temperature dependence. This absorbed fluence value can be considered large when compared to the typical fluences that are sufficient for driving $\text{La}_{2-x}\text{Sr}_x\text{CuO}_4$ and $\text{Bi}_2\text{Sr}_2\text{CaCu}_2\text{O}_{8+x}$ into the normal state. To explain the discrepancy, we recall that: i) 123-family of cuprates has been demonstrated to tolerate high levels of absorbed laser fluence before the total vaporization of the condensate takes place¹⁷; ii) our estimate of the absorbed fluence is performed outside the cryostat by positioning a beam profiler in the focal point of the pump and probe beams; an imprecise positioning of the sample in the focal region may lead to an error of $\sim 20\%$ in the estimated fluence when the sample is maintained inside the cryostat.

To highlight the fluence value at which the total vaporization of the condensate occurs, we also explore the fluence regime $> 0.35 \text{ mJ/cm}^2$. Figure S4 displays the color-coded maps of $\Delta R/R$ at 10 K and 300 K for some representative values of the absorbed fluence (indicated in the labels). As a larger number of pump photons are delivered onto the sample, the spectral response of NBCO at 10 K starts displaying a positive contribution around 2.10 eV and strongly differs from the lower-fluence regime. The rise of this spectroscopic feature around 2 mJ/cm^2 represents the signature of a highly thermal nonequilibrium state driven by the pump pulse, which resembles the signal measured at 300 K. We also remark that, in independent measurements on YBCO thin films at 5 K¹⁸, a similar response was observed for a fluence of 0.113 mJ/cm^2 . This discrepancy can be again related to an imprecise estimate of the fluence absorbed by our sample. Alternatively, one can speculate that our NBCO single crystal has a high critical fluence threshold for the complete vaporization of the condensate. Irrespective of the absolute fluence absorbed by the crystal, the arguments provided assure that the temperature dependence reported in the following paragraph bears the unambiguous fingerprints of the QP response of the SC state.

The linearity in the normal state at 300 K is instead maintained over a wider absorbed fluence range, as previously observed in literature for $\text{Bi}_2\text{Sr}_2\text{CaCu}_2\text{O}_{8+x}$ ¹⁹.

B. Temperature dependence

Figure S5 reports the complete temperature dependence of the in-plane transient reflectivity $\Delta R/R$ as a function of the probe photon energy and the delay time

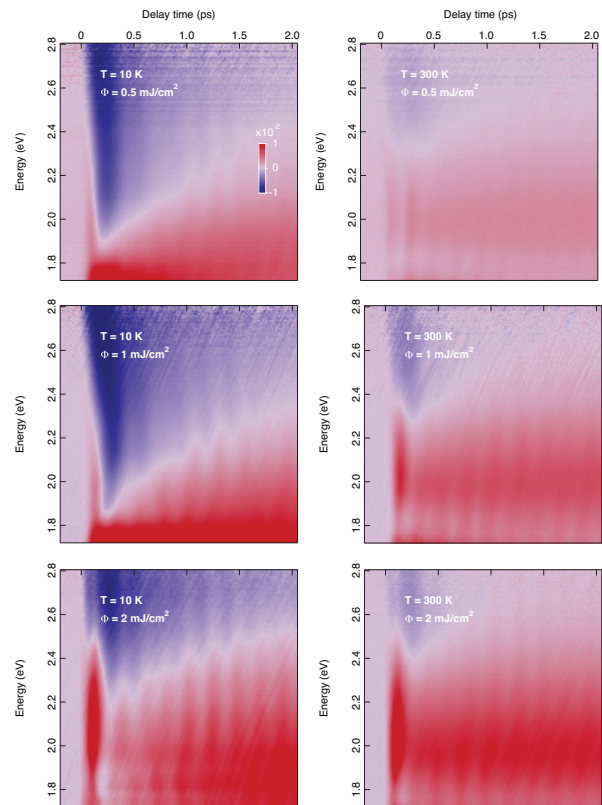


FIG. S4. Fluence dependence of the transient reflectivity $\Delta R/R$, displayed as a function of the probe photon energy and of the time delay between pump and probe. The temperatures of 10 K and 300 K and the values of the absorbed fluence of 0.5 mJ/cm^2 , 1 mJ/cm^2 and 2 mJ/cm^2 are indicated in the labels.

between pump and and probe. The temperatures are reported in the labels.

C. Global fit analysis

We performed a global fit analysis of $\Delta R/R$ as a function of time. Eleven temporal traces have been selected from each map of the temperature dependence and fitted

$$f(t) = f_H(t) + f_{PG}(t) + f_{QP}(t) = e^{\frac{-t^2}{\tau_{R1}}} * A_H e^{-\frac{t-t_{D1}}{\tau_H}} + e^{\frac{-t^2}{\tau_{R2}}} * \left[A_{PG} e^{-\frac{t-t_{D2}}{\tau_{PG}}} + A_{QP} e^{-\frac{t-t_{D2}}{\tau_{QP}}} \right] \quad (2)$$

where A_H , A_{PG} and A_{QP} are the amplitudes of the three exponential functions; τ_{R1} and τ_{R2} are the rise times of the exponential functions; τ_H , τ_{PG} and τ_{QP} are the relaxation constants of the three exponentials; t_{D1} and t_{D2} are delay parameters with respect to the zero time.

Depending on the temperature, the extracted values for the time constants varied in the following way:

$\tau_{PG} = 150 \div 250$ fs ($\pm 4 \div 9$ fs), $\tau_{QP} = 4 \div 6$ ps ($\pm 0.65 \div 1.6$ ps), $\tau_H = 34 \div 50$ ps ($\pm 10 \div 21$ ps).

These three timescales match those reported by all pump-probe experiments on cuprates (see the references cited in the main text). The large uncertainty on the τ_H is due to the limited temporal window probed in our experiment. The function reported in Eq. (2) allowed to capture both the early temporal dynamics, represented by the resolution-limited positive rise, and the delayed negative contribution whose maximum amplitude occurs around 200 fs. In such a model function, the exponential term with relaxation constant τ_H embodies the response of localized carriers which remained trapped in a long-lived state^{20,21}; the two exponential terms with delay t_{D2} represent the conventional PG and QP response reported in all pump-probe spectroscopy experiments. We remark that simpler fit functions (not accounting for the two separate rise times and the two separate delays) could not result in a convergent fit. Hence, although the microscopic explanation for the long-lived component might

simultaneously by imposing the same time constants.

Different models with gradual complexity have been tried to obtain a satisfactory fit of the incoherent response at low temperature. The easiest model which was capable to reproduce the experimental data across the broad spectral range consists of three distinct exponential functions. No converging fit was obtained by using two exponential functions. The function that was used for fitting the data is:

not be related to an ultrafast localization of charge carriers, we first make use of Eq. (2) for fitting the data in an accurate way, as it represents the simplest fit function with the smallest number of free parameters. Below in this paragraph, we also show that another fit function can be used to successfully reproduce our data at all temperatures, by describing a long-lived bolometric response. At high temperatures, the data were instead fitted using two exponential functions, in agreement with the results obtained in the literature of pump-probe spectroscopy for the analysis of the normal state (which is cited in the main text).

Figure S6 displays the experimental temporal traces cut around 1.90 eV, together with the results of the global fit analysis. In each panel the result of the fit has been superimposed to the experimental data and the decomposition of the final fit function into its separate contributions is reported as well. The results are shown at different temperatures (10, 85, 90, 95, 100, 110, 130, 150 K).

In Fig. S7 we prove the stability of the global fit across the whole probed spectral region. Every panel shows the 11 experimental temporal traces (colored traces) in which the broad spectrum has been cut, together with the results of the global fit (black curves superimposed). The red curve at the top of each graph is the temporal trace at 1.80 eV, while the purple curve at the bottom is the temporal trace at 2.70 eV. We observe that the model used to fit the data is very accurate across the broad spectrum and catches the detailed features characterizing the early dynamics of the transient response.

To highlight the breakdown of the two-component scenario in the fit of the data at 130 K (*i.e.* well above $T_C = 93.5$ K), we show in Fig. S8 a comparison between the best fitted responses using two (violet curve) and three (red curve) components. It is evident that only a three-component scenario can satisfactorily reproduce the data, thus implying the presence of a ps-lasting QP response (albeit small).

As anticipated above, we also used a second approach for fitting the experimental data, which involves a Gaussian pulse-like contribution for capturing the early dy-

ε_{inf}		2.1			
ω_0	cm^{-1}	ω_p	cm^{-1}	γ	cm^{-1}
0		19518		2317	
11142		22300		19441	
21275		8530		5934	
35669		31244		17456	
47407		17442		7578	
61073		53520		12982	

TABLE S1. Typical values for the static Drude-Lorentz model, in this case for the data at 15 K. The table lists the high-frequency dielectric constant ε_{inf} , the eigenfrequencies ω_0 , the plasma frequencies ω_p and the linewidths γ .

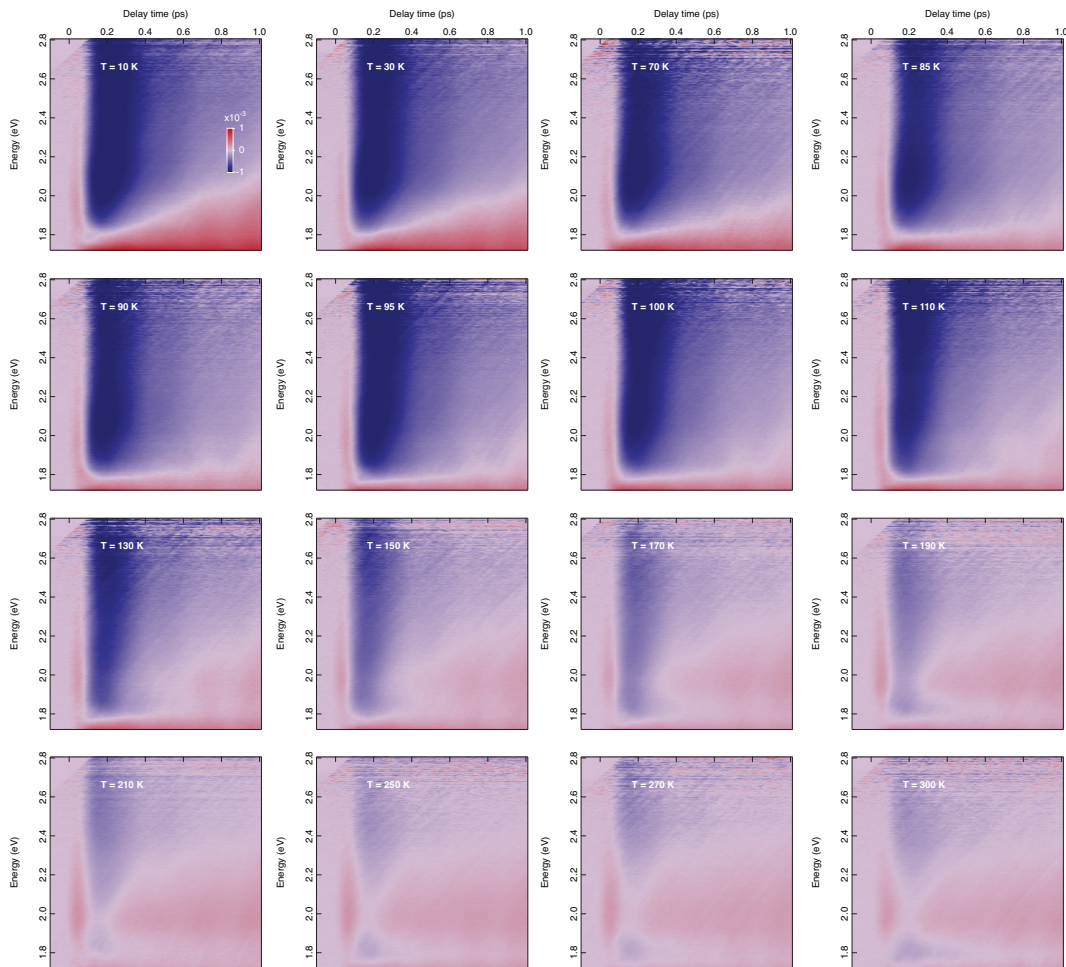


FIG. S5. Measured temperature dependence of the transient reflectivity $\Delta R/R(\tau, E)$, displayed as a function of the probe photon energy and of the time delay between pump and probe. The absorbed fluence is 0.3 mJ/cm^2 and the temperatures are listed as labels in the maps.

namics, a slowly rising long-lived component and the two delayed exponential functions of the previous model. The separate contributions are depicted in Fig. S9(a) for the temporal trace at 1.90 eV at 10 K . In this case, the Gaussian pulse is used to model the initial metallic contribution setting after the interaction of the pump with the sample, following the model of Okamoto *et al.*²². The delayed negative exponential functions still embody the PG and QP response, decaying with time constants τ_{PG} and τ_{QP} . The long-lived component instead corresponds to the bolometric (heating) response of the sample, which sets after the thermalization of the excited carriers has occurred. Although the use of this fit function led to a satisfactory description of the experimental data, the number of free parameters was larger than the function proposed in the previous model. In any case, this second fitting approach did not change the outcome of our analysis in a substantial way (Fig. S9(b)).

D. Transient optical conductivity

To extract the transient optical conductivity $\Delta\sigma/\sigma(\omega, t)$ from the transient reflectivity $\Delta R/R(\omega, t)$, we first calculate the static reflectivity R from the static SE data in the range between 5000 cm^{-1} (0.62 eV) and 52000 cm^{-1} (6.45 eV). With this quantity, we obtain the momentary reflectivity $R(\omega)$ in the range between 14100 cm^{-1} (1.75 eV) and 23250 cm^{-1} (2.88 eV) by multiplying $\Delta R/R(\omega, t)$ at a fixed delay time t' with the static reflectivity.

To obtain a reliable fit of the transient conductivity, we start by fitting a Drude-Lorentz model to the static conductivity σ at each temperature T . The model comprises a Drude peak and three Lorentz oscillators. An additional oscillator at high energies compensates for spectral weight outside our energy range. Typical values for the static model are given in table S1. The static model can now be fitted sequentially to the momentary reflectivity

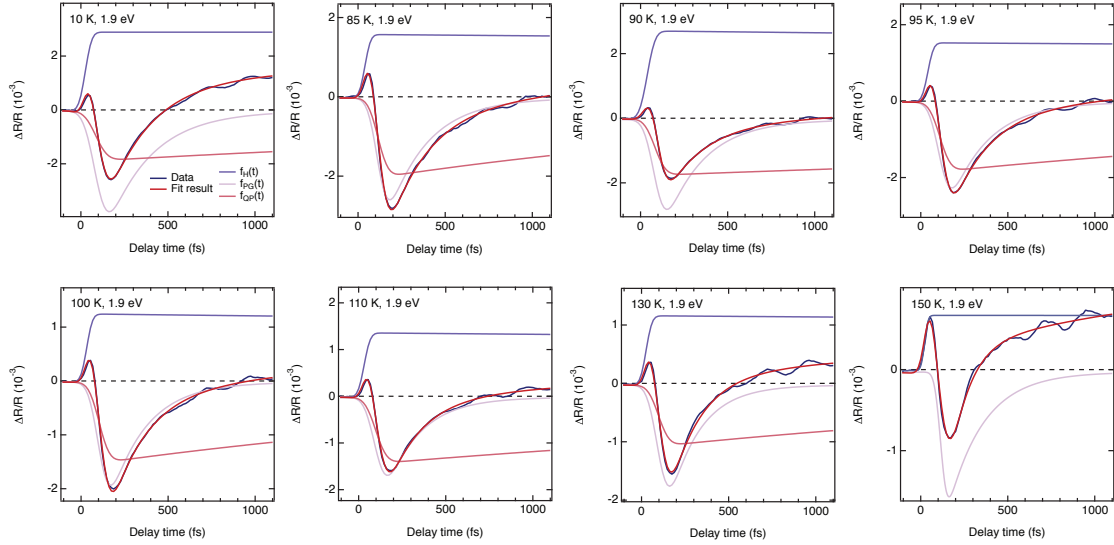


FIG. S6. Results of the global fit analysis on the temporal trace at 1.9 eV for different temperatures (10, 85, 90, 95, 100, 110, 130, 150 K). The experimental data are reported in blue, the results of the global fit in red. The remaining curves represent the separate contributions to the fitting function.

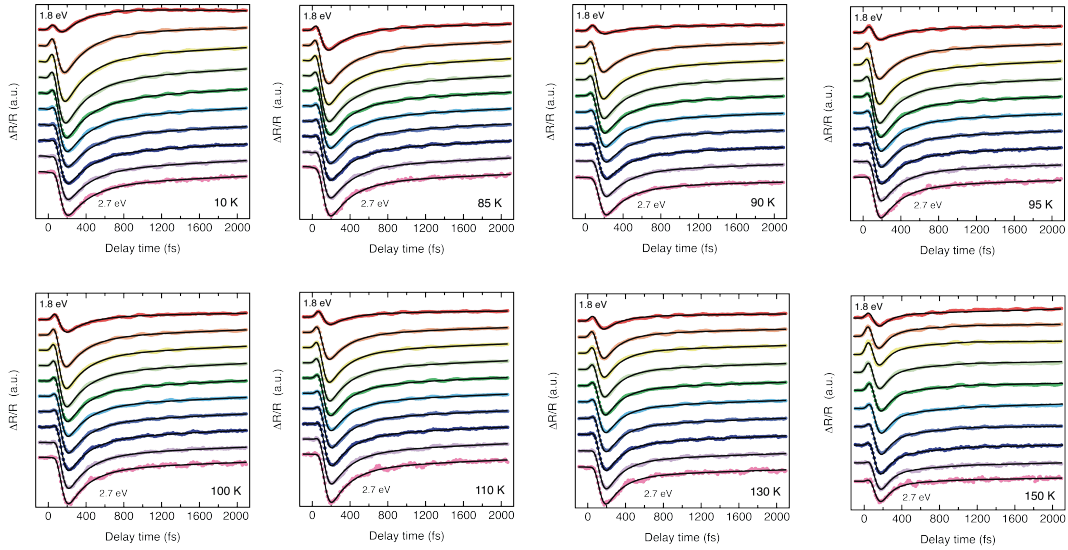


FIG. S7. Global fit analysis of the temporal traces at 10, 85, 90, 95, 100, 110, 130, 150 K for different probe photon energies (from 1.80 eV at the top of the graphs to 2.70 eV at the bottom, with a constant spacing of 0.10 eV).

$R(\omega)$ at each delay time t' , yielding the momentary conductivity $\sigma(\omega, t')$. To improve the reliability of the fit, the model is fitted simultaneously to the transient momentary reflectivity inside our probing range as well as to the static reflectivity outside the probed range, between 5000 cm^{-1} (0.62 eV) and 13800 cm^{-1} (1.71 eV) and between 23800 cm^{-1} (2.95 eV) and 52000 cm^{-1} (6.45 eV). The use of the static reflectivity outside the probed spec-

trum is justified by the fact that the overall changes in the conductivity are considered small (on the order of the transient reflectivity), meaning that the missing transient data can be approximated by the static data. This approximation constitutes a technical trick, and the fit result is considered valid only inside the probed range. Note that there is a small gap in between the transient reflectivity and the static reflectivity, which helps to avoid

discontinuities. In a final step, the momentary conductivity spectra $\sigma(\omega, t')$ are recombined into the full map $\sigma(\omega, t)$, and the transient conductivity $\Delta\sigma/\sigma(\omega, t)$ is obtained by dividing by the static conductivity $\sigma(\omega)$.

Figures S10(a)-(b) display the temporal traces and the transient spectrum of $\Delta\sigma_1/\sigma_1$ at 10 K, which have been cut from the map displayed in Fig. 5 of the main text. Figures S10(c)-(d) show the corresponding temporal traces and the transient spectrum of $\Delta\sigma_2/\sigma_2$.

We selected ten temporal traces across the broadband spectral range and we performed a global fit analysis, by imposing the same model used for the global fit of $\Delta R/R$. This global fit allowed us to isolate the spectral fingerprints of the three separate components emerging in our nonequilibrium experiment. These spectral components are shown in Fig. S11(a)-(b), in which we used the same nomenclature reported in Eq. (2). We observe that A_H provides a positive contribution to $\Delta\sigma_1/\sigma_1$, while A_{PG} and A_{QP} are at the origin of the decreased $\Delta\sigma_1/\sigma_1$ which is dominating in the traces and spectra of Fig. S10(a).

Here, we can contribute to the discussion concerning the long-live component, which has been previously assigned either to a pump-induced heating effect or as the signature of an excited-state absorption from localized (polaronic) carriers^{20,21}. Indeed, in Fig. S12 we compare the effect produced on σ_1 by this long-lived component in the nonequilibrium experiment and the variation in σ_1 provided by a static increase of the crystal temperature (from 10 to 30 K). We observe an excellent matching between the two trends, which suggests that the long-lived component corresponds to the bolometric response of our sample. Notice that this assignment implies that the correct model to fit the data is the one described in Fig. S9(a), as the rise of the bolometric response is strictly correlated to the thermalization of the hot charge carriers after the initial excitation.

Finally, in Fig. S13, we report the effects produced by

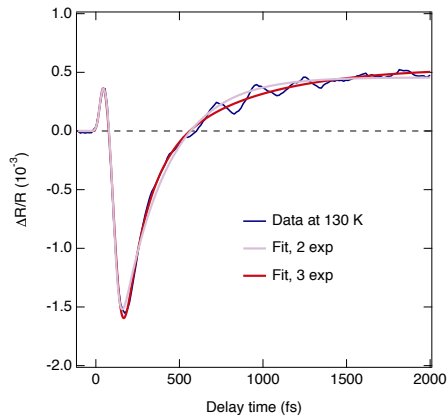


FIG. S8. Comparison between the best fitted responses using two (violet curve) and three (red curve) components. The experimental data at 130 K are reported as a blue curve.

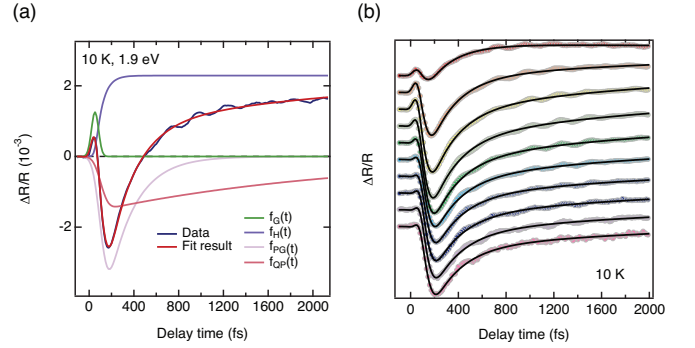


FIG. S9. (a) Results of the global fit analysis on the temporal trace at 1.90 eV and 10 K. The experimental data are reported in blue, the results of the global fit in red. The remaining curves represent the separate contributions to the fitting function. (b) Global fit analysis of the temporal traces at 10 K for different probe photon energies (from 1.80 eV at the top of the graphs to 2.70 eV at the bottom, with a constant spacing of 0.10 eV).

each separate component on the equilibrium σ_1 . In each panel, the variation occurring in σ_1 has been multiplied by a factor 5 to make the change distinguishable. As explained in the main text, both the PG and QP responses remove SW in the visible region, redistributing it most likely to lower energy.

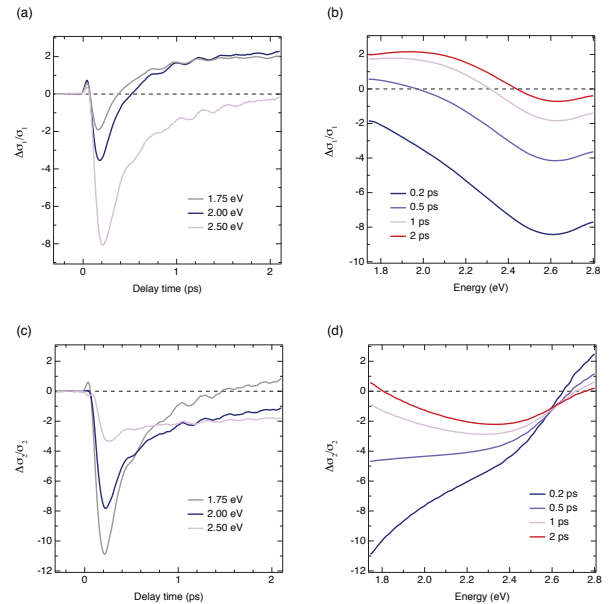


FIG. S10. (a,c) Temporal traces of $\Delta\sigma_1/\sigma_1$ ($\Delta\sigma_2/\sigma_2$) at 10 K for fixed probe photon energies of 1.75 eV, 2.00 eV and 2.50 eV (b,d) Transient spectrum of $\Delta\sigma_1/\sigma_1$ ($\Delta\sigma_2/\sigma_2$) at 10 K for selected delay times of 0.2, 0.5, 1 and 2 ps.

E. Coherent phonons

We also tracked the amplitude of the Ba and Cu modes as a function of the probe photon energy, by performing a Fourier transform analysis of the residuals from the global fit. Thanks to the broadband probe, this methodology allows to map the Raman matrix element for each Raman-active mode which is coherently excited in the pump-probe experiment^{5,11}. In Fig. S14 we report the separate Raman matrix elements for the Ba (blue curve) and Cu (red curve) modes at 10 K.

We observe that at 2.00 eV the Ba mode intensity is larger than the Cu mode intensity by a factor 1.7. This is consistent with the results reported by single-wavelength pump-probe spectroscopy at 2.00 eV, in which the low-temperature signal was found to be dominated by the contribution of the Ba mode²³. The general trend described by our Raman matrix elements also agrees with early spontaneous Raman scattering experiments performed at varying laser photon energies²⁴. Finally, it is worth to underline the resonant behaviour displayed by the Cu mode for probe photon energies below 1.80 eV, *i.e.* outside our probed spectral range. This finds a possible

explanation in the proximity of the spectroscopic feature at 1.40 - 1.77 eV (Fig. S2(a)), which has been associated with the reminiscence of the charge-transfer excitation in the CuO₂ planes. We remark that the shape of the determined Raman matrix elements are very similar to the ones reported in Ref.¹¹ for OP YBCO.

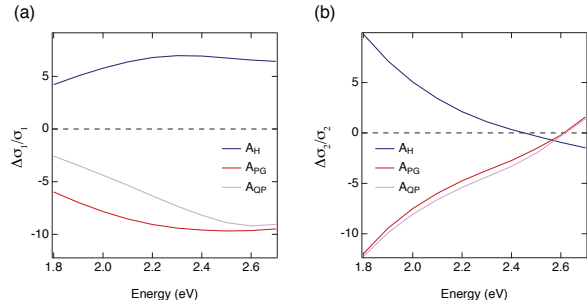


FIG. S11. Transient optical conductivity spectra of the three components obtained from the global fit analysis.

(a) $\Delta\sigma_1/\sigma_1$; (b) $\Delta\sigma_2/\sigma_2$.

- ¹ S. I. Schlachter, U. Tutsch, W. H. Fietz, K.-P. Weiss, H. Leibrock, K. Grube, T. Wolf, B. Obst, P. Schweiss, and H. Wühl, *Int. J. Mod. Phys. B* **14**, 3673 (2000).
- ² C. Bernhard, J. Humlíček, and B. Keimer, *Thin Solid Films* **455**, 143 (2004).
- ³ R. M. A. Azzam and N. M. Bashara, *Ellipsometry and Polarized Light* (North-Holland, sole distributors for the USA and Canada, Elsevier Science Publishing Co., Inc., 1987).
- ⁴ J. Humlíček and C. Bernhard, *Thin Solid Films* **455**, 177 (2004).
- ⁵ A. Mann, E. Baldini, A. Tramontana, E. Pomjakushina, K. Conder, C. Arrell, F. van Mourik, J. Lorenzana, and F. Carbone, *Phys. Rev. B* **92**, 035147 (2015).
- ⁶ L. Yu, D. Munzar, A. V. Boris, P. Yordanov, J. Chaloupka, T. Wolf, C. T. Lin, B. Keimer, and C. Bernhard, *Phys. Rev. Lett.* **100**, 177004 (2008).
- ⁷ S. L. Cooper, D. Reznik, A. Kotz, M. A. Karlow, R. Liu, M. V. Klein, W. C. Lee, J. Giapintzakis, D. M. Ginsberg, and B. W. Veal, *Phys. Rev. B* **47**, 8233 (1993).
- ⁸ J. Bäckström, D. Budelmann, R. Rauer, M. Rübhausen, H. Rodriguez, and H. Adrian, *Phys. Rev. B* **70**, 174502 (2004).
- ⁹ J. Lorenzana and G. Seibold, *Phys. Rev. Lett.* **90**, 066404 (2003).
- ¹⁰ J. Kircher, M. K. Kelly, S. Rashkeev, M. Alouani, D. Fuchs, and M. Cardona, *Phys. Rev. B* **44**, 217 (1991).
- ¹¹ D. Fausti, F. Novelli, G. Giovannetti, A. Avella, F. Cilento, L. Patthey, M. Radovic, M. Capone, and F. Parmigiani, *arXiv:1408.0888* (2014).
- ¹² M. Rübhausen, A. Gozar, M. V. Klein, P. Guptasarma, and D. G. Hinks, *Phys. Rev. B* **63**, 224514 (2001).
- ¹³ H. J. A. Molegraaf, C. Presura, D. van der Marel, P. H. Kes, and M. Li, *Science* **295**, 2239 (2002).

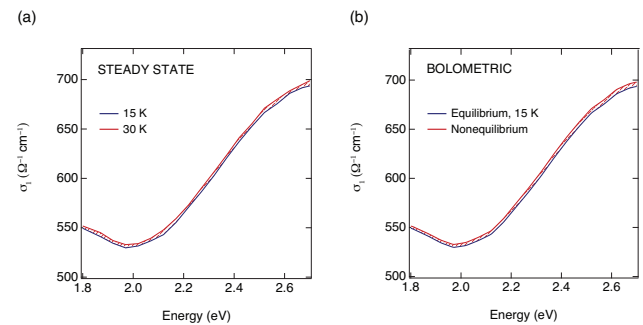


FIG. S12. (a) Steady-state optical conductivity measured by SE in the visible range at 15 K (blue curve) and 30 K (red curve). (b) Effect produced on the equilibrium σ_1 (represented in blue) by the long-lived component in the transient signal. This can be identified as the bolometric response of the crystal after photoexcitation.

- ¹⁴ A. V. Boris, N. N. Kovaleva, O. V. Dolgov, T. Holden, C. T. Lin, B. Keimer, and C. Bernhard, *Science* **304**, 708 (2004).
- ¹⁵ T. D. Stanescu and P. Phillips, *Phys. Rev. Lett.* **91**, 017002 (2003).
- ¹⁶ F. Carbone, A. B. Kuzmenko, H. J. Molegraaf, E. Van Heumen, V. Lukovac, F. Marsiglio, D. van der Marel, K. Haule, G. Kotliar, and H. Berger, *Phys. Rev. B* **74**, 064510 (2006).
- ¹⁷ A. Pashkin, M. Porer, M. Beyer, K. W. Kim, A. Dubroka,

- C. Bernhard, X. Yao, Y. Dagan, R. Hackl, and A. Erb, Phys. Rev. Lett. **105**, 067001 (2010).
- ¹⁸ F. Novelli, *In search of selective excitations for studying out-of-equilibrium properties in strongly correlated electron systems and high temperature superconductors*, Ph.D. thesis, University of Trieste (2013), <https://www.openstarts.units.it/dspace/handle/10077/8588>.
- ¹⁹ C. Giannetti, G. Coslovich, F. Cilento, G. Ferrini, H. Eisaki, N. Kaneko, M. Greven, and F. Parmigiani, Phys. Rev. B **79**, 224502 (2009).
- ²⁰ T. N. Thomas, C. J. Stevens, A. J. S. Choudhary, J. F. Ryan, D. Mihailovic, T. Mertelj, L. Forro, G. Wagner, and J. E. Evetts, Phys. Rev. B **53**, 12436 (1996).
- ²¹ C. J. Stevens, D. Smith, C. Chen, J. F. Ryan, B. Podobnik, D. Mihailovic, G. A. Wagner, and J. E. Evetts, Phys. Rev. Lett. **78**, 2212 (1997).
- ²² H. Okamoto, T. Miyagoe, K. Kobayashi, H. Uemura, H. Nishioka, H. Matsuzaki, A. Sawa, and Y. Tokura, Phys. Rev. B **83**, 125102 (2011).
- ²³ W. Albrecht, T. Kruse, and H. Kurz, Phys. Rev. Lett. **69**, 1451 (1992).
- ²⁴ B. Friedl, C. Thomsen, H.-U. Habermeier, and M. Cardona, Sol. State Comm. **78**, 291 (1991).

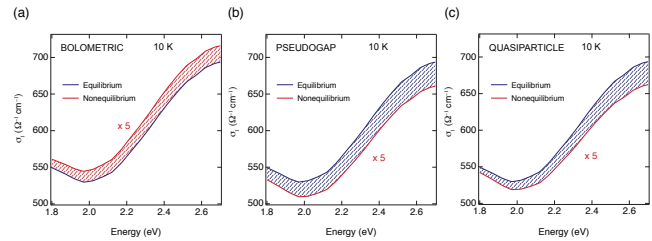


FIG. S13. Effects produced on the equilibrium σ_1 (represented as blue lines) by (a) the bolometric, (b) the PG and (c) the QP responses. The nonequilibrium σ_1 is drawn as a red curve and the added (removed) SW is depicted by the red (blue) filled area.

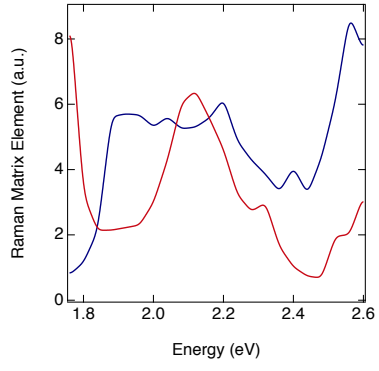


FIG. S14. Raman matrix elements of the Ba (blue curve) and Cu (red curve) modes at 10 K, as determined from the Fourier transform analysis as a function of the probe photon energy.